It has been proposed that the large slow region in the mantle beneath the central Pacific, identified in some early work (*3*) and observed in all tomographic models, is related to a megaplume generated by thermal boundary layer instabilities at the CMB (*17*). The large negative amplitude we infer in this region could be in part related to partial melt, as has been proposed to explain the ultralow velocities observed in some parts of this region (*18*). Some chemical heterogeneity, possibly involving core material, may be present as well (*19*). Our forward modeling predicts that the base of this possible upwelling is rather wide and that the plume narrows as it extends into the lower mantle, consistent with the spectral content of tomographic models, which shows a shift from red (large wavelengths) to white when ascending from the D″ region into the bulk lower mantle (*12, 13*). The plume also appears to be deflected to the southwest as it rises, indicating possible entrainment in the general circulation mantle flow (*20*).

The high-velocity region documented by our modeling represents a contrast of about 7 to 8% with respect to adjacent "hot" mantle and cannot be explained by thermal effects alone. A portion of ancient slab lying at the CMB is not likely to be responsible for this velocity contrast because reconstructions of ancient subduction zones do not predict the presence of remnant lithosphere in this part of D″ (*21*), and such a fossil slab might not produce a sufficient velocity contrast (*22*). This fast and localized anomaly could represent a high-velocity product of the decomposition of perovskite at temperatures and pressures corresponding to the lowermost mantle (*23*) or of core-mantle reactions (*19, 24*), and it may be related to the selective entrainment of chemically distinctive material into the thermal plume (*25*). Because significant shear wave splitting has been observed for waves traveling through that region (*6, 8*), the large velocity contrast that we have observed could also be related to anisotropy, whether it is due to lattice preferred orientation of anisotropic minerals (*24*) or laminar fabrics that would present themselves at different angles to the through-going SH waves, respectively, in the slow and fast regions. Finally, the block of fast material "sitting" on the CMB could be responsible for the intermittent reflections observed at the top of D″ in this region (*26*).

References and Notes

1. D. E. Loper and T. Lay, *J. Geophys. Res.* **100**, 6397 (1995).
2. T. Lay and D. V. Helmberger, *Geophys. J. R. Astron. Soc.* **75**, 799 (1983).
3. J. Schweitzer and G. Muller, *Geophys. Res. Lett.* **13**, 1529 (1986).
4. E. J. Garnero and D. V. Helmberger, *J. Geophys. Res.* **98**, 8225 (1993); M. Sylvander and A. Souriau, *Phys. Earth. Planet. Inter.* **94**, 1 (1996); M. E. Wysession, *Nature* **382**, 244 (1996); J. Ritsema, E. Garnero, T. Lay, *J. Geophys Res.* **102**, 20395 (1997).
5. L. Bréger, B. Romanowicz, L. Vinnik, *Geophys. Res. Lett.* **25**, 5 (1998).
6. L. Vinnik, L. Bréger, B. Romanowicz, *Nature* **393**, 564 (1998).
7. J. M. Kendall and P. G. Silver, *ibid.* **381**, 409 (1996).
8. J. Ritsema, E. J. Garnero, H. Benz, *Geophys. Res. Lett.* **25**, 1229 (1998).
9. J. E. Vidale and M. A. Hedlin, *Nature* **391**, 682 (1998).
10. L. Wen and D. V. Helmberger, *Science* **279**, 1701 (1998).
11. R. A. W. Haddon and G. G. R. Buchbinder, *Geophys. Res. Lett.* **14**, 891 (1987); V. F. Cormier, *J. Geophys.* **57**, 14 (1985); X. -F. Liu, J. Tromp, A. Dziewonski, *Earth Planet. Sci. Lett.*, in press.
12. S. Grand, R. van der Hilst, S. Widiyantoro, *G.S.A. Today* **7**, 1 (1997); X.-F. Liu, W.-J. Su, A. M. Dziewonski, *Eos* (spring suppl.) **75**, 232 (1994); G. Masters, S. Johnson, G. Laske, H. Bolton, *Philos. Trans. R. Soc. London* **354**, 1385 (1996).
13. X. -D. Li and B. Romanowicz, *J. Geophys Res.* **101**, 22245 (1996).
14. A. Dziewonski and D. L. Anderson, *Phys. Earth Planet. Int.* **25**, 297 (1981).
15. A finite difference (FD) modeling approach is desirable to forward model not only travel times but also waveforms in 3D. Such modeling is computationally heavy and not well suited for a trial and error approach unless the model space is restricted by using independent constraints. On the other hand, travel times can be modeled by using much more expedient ray approaches, which can provide well-constrained starting models for the more refined FD waveform modeling. We have computed synthetic travel time residuals for available tomographic models by using ray theory. The ray tracing was done in the spherically symmetric PREM model (*13*). We verified that, within the accuracy of the measurements (1 to 2 s), the results obtained for *S* and *SKS* were consistent with computations made with an acoustic 2D FD SH algorithm [J. E. Vidale, thesis, California Institute of Technology (1987)].
16. Large residuals (7 to 8s) are systematically observed at short distances (80° to 90°) on some profiles, implying very low velocities up to about 1000 km above the CMB. Tradeoffs between strength of anomalies and extent of the anomalous zone do not allow us to uniquely determine how much further above the CMB the anomaly extends. The model shown is, however, consistent with tomographic models, which show a significant drop in rms heterogeneity above that depth.
17. F. D. Stacey and D. E. Loper, *Phys. Earth. Planet. Inter.* **33**, 45 (1983); N. H. Sleep, *J. Geophys. Res.* **95**, 6715 (1990); P. F. Thompson and P. J. Tackley, *Geophys. Res. Lett.* **25**, 1999 (1998).
18. Q. Williams and E. J. Garnero, *Science* **273**, 1528 (1996).
19. E. Knittle and R. Jeanloz, *ibid.* **251**, 1438 (1991).
20. B. Steinberger and R. J. O'Connell, *Geophys. J. Int.* **132**, 412 (1998).
21. C. Lithgow-Bertelloni and M. A. Richards, *Rev. Geophys.* **36**, 27 (1998).
22. M. E. Wysession *et al.*, in *The Core-Mantle Boundary*, M. Gurnis, B. A. Buffett, E. Knittle, M. E. Wysession, Eds. (American Geophysical Union, Washington, DC, 1998), pp. 273–297.
23. L. S. Dubrovinsky *et al.*, *Nature* **388**, 362 (1998).
24. L. Stixrude, in *The Core-Mantle Boundary*, M. Gurnis, B. A. Buffett, E. Knittle, M. E. Wysession, Eds. (American Geophysical Union, Washington, DC, 1998), pp. 83–96; S. Karato, *Earth Space Sci.*, in press.
25. L. H. Kellogg and S. D. King, *Geophys. Res. Lett.* **20**, 379 (1993).
26. E. J. Garnero, D. V. Helmberger, G. Engen, *ibid.* **15**, 609 (1988).

27. We thank Ed Garnero for making his data available to us and for helpful discussions and two anonymous referees for constructive reviews. This work was funded by IGPP/LLNL grant 98-GS014. This is Seismological Laboratory contribution 98-04.

1 July 1998; accepted 15 September 1998

Pressure-Induced Landau-Type Transition in Stishovite

Denis Andrault,* Guillaume Fiquet, François Guyot, Michael Hanfland

A Rietveld structural analysis of stishovite, with angle-dispersive x-ray diffraction synchrotron source at the European Synchrotron Radiation Facility, confirmed a $CaCl_2$ form of stishovite distortion at 54 ± 1 gigapascals but confirmed no further phase transformation up to 120 gigapascals. The deviatoric stress that is usually encountered at such pressures was relaxed after yttrium-aluminum-garnet–laser heating. A single Birch-Murnaghan equation of state fits volumes of stishovite and a $CaCl_2$ form, showing that the tetragonal distortion occurs without a substantial change in volume. At the 54-gigapascal transition, the pressure-induced lattice modifications were similar to those found in a Landau-type temperature-induced transition. It is proposed that, above the transition pressure, the critical temperature increases above 300 kelvin, so that the lower entropy form becomes stable.

There is no closely packed compact ionic arrangement for metal dioxides. The most common dense form of BO_2 compounds (where B is Si, Ti, Ge, and so forth) is rutile, in which the oxygen sublattice can be seen as largely distorted face-centered cubic and in which only one of the two octahedral sites is filled by silicon (Fig. 1). Rutile can also be compared to the ABO_3 perovskite-type structure (where AB is MgSi, CaTi, SrZr, and so forth), in which the lack of the A cation would be balanced by a modification of the octahedral links, thus reducing the size of the vacant polyhedra. There are several other dense forms of the BO_2 compounds because

D. Andrault, Laboratoire des Géomatériaux, Institut de Physique du Globe, Paris 75252, France. G. Fiquet, Laboratoire de Géologie, Ecole Nationale Supérieure de Lyon, Lyon 69364, France. F. Guyot, Laboratoire de Minéralogie-Cristallographie, Université Paris VII, Paris 75252, France, and Institut de Physique du Globe, Paris 75252, France. M. Hanfland, European Synchrotron Radiation Facility, Grenoble 38043, France.

*To whom correspondence should be addressed.

comparable energies are found for slightly different octahedral interlinks. For example, six polymorphs have been reported for PbO_2 between room pressure and 47 GPa (*1*). The sequence of the SiO_2 phase transformations down to the core-mantle boundary (CMB) of Earth needs further analysis because it can affect the lower mantle composition through a possible breakdown of silicate perovskite, the major lower mantle mineral (*2*).

Silica could adopt a $CaCl_2$-type post-stishovite structure, as suggested by several experiments with x-ray diffraction (*2–4*) or Raman spectroscopy (*5*). Several ab initio structure simulations also indicated a $CaCl_2$-type post-stishovite distortion, from pressures of 45 to 200 GPa (*6–9*). Other studies also proposed the occurrence of post-$CaCl_2$-type polymorphs at lower mantle pressures ($P <$ 130 GPa). An α-PbO_2 structure type was proposed for SiO_2 from high-pressure x-ray diffraction experiments (*Pnc*2) (*2*) and was observed in a shocked meteorite (*Pbcn*) (*10*). The possible stability of such a polymorph is supported by recent calculations (*2*, *7*, *8*). Finally, the densest form of BO_2 compounds consists of a Pa-modified fluorite-type structure (*11*, *12*), but this polymorph has not been observed for SiO_2 and is only expected to occur at pressures of ~150 GPa, which is much higher than the pressure of the CMB (*6*).

Synthetic crystals of quartz were finely ground, mixed with platinum black, and loaded in an 80-μm hole in a rhenium gasket that had been previously indented with 200–300-μm-bevel diamonds. The pressure was measured within the x-ray spot, according to the known equation of state (EOS) of Pt (*13*). The use of Pt avoids possible artifacts that are related to the pressure gradient in the sample chamber, and pressure measurement errors are estimated to be <3%. After each pressure increase, the sample chamber was slowly scanned by the infrared radiation of a multimode-regulated yttrium-aluminum-garnet laser. This laser-annealing technique efficiently relaxes the sample stresses and results in a quasi-hydrostatic pressure in the pressure chamber, which improves the quality of the x-ray diffraction spectra (*14–17*). The annealing technique may favor the formation of high-temperature polymorphs of the sample, which would be quenched upon cooling.

Angle-dispersive x-ray diffraction spectra were recorded at the insertion device 9 (ID9) beamline of the European Synchrotron Radiation Facility (ESRF). A water-cooled Si (111) bent Laue monochromator was used to produce a bright monochromatic x-ray beam at a wavelength of 0.4561 Å. Vertical and horizontal focusing were achieved with a spherical mirror and a monochromator, respectively. The x-ray flux on a 15-by-15-μm spot allowed the acquisition of diffraction spectra on an imaging plate in ~10 min. The two-dimensional images were integrated with the Fit2d code (*18*). Lebail profile refinements with the program package GSAS (*19*) were applied to all diffraction patterns to extract cell parameters and volumes for SiO_2 and Pt. In the last step of data processing, the code was changed to the Rietveld-refinement mode, to compare experimental intensities with those that were calculated for different structural models.

X-ray diffraction spectra up to 53.2 GPa (Fig. 2A) can be explained as a mixture of Pt and SiO_2 (except for peaks from 2.3 to 2.4 Å, which can be explained by traces of the Re gasket). The spectrum that was recorded at 54.8 GPa shows slight modifications that are

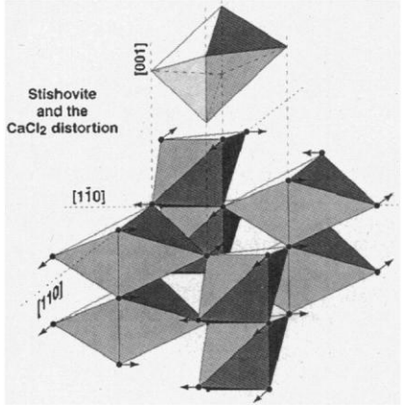

Fig. 1. Dense atomic arrangement for silica. Half of the octahedral sites of the oxygen sublattice are filled with Si atoms. SiO_6 octahedra show four equatorial and two polar Si–O bonds. The $CaCl_2$-type stishovite distortion occurs when oxygen escapes from the diagonal of the (*a*, *b*) plane, thus changing the symmetrical arrangement from tetragonal to orthorhombic.

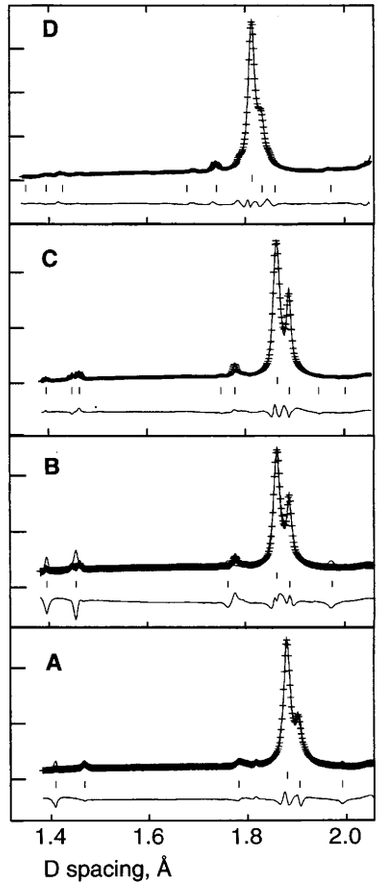

Fig. 2. Selected region of Rietveld fits showing the occurrence of new diffraction lines that fit with a $CaCl_2$-type SiO_2 distortion above 54 GPa. Structural models are (**A**) stishovite and Pt at 46.8 GPa, (**B**) stishovite and Pt at 63 GPa, (**C**) $CaCl_2$-type SiO_2 and Pt at 63 GPa, and (**D**) $CaCl_2$-type SiO_2 and Pt at 120 GPa. Dashes and upper and lower solid lines represent experimental, modeled, and difference spectra, respectively.

Table 1. Experimental (Exp.) and calculated (Calc.) d_{hkl} Bragg lines with cell parameters of SiO_2 (*P*4_2/*mnm*) and $CaCl_2$-type SiO_2 (*Pnnm*) at 53.2 and 63 GPa, respectively. *V*, volume; numbers in parentheses are uncertainties in measured parameters; *, SiO_2 lines superimposed with Pt lines; **, lines found with negligible intensity.

d_{hkl}	Cell parameters	Stishovite		$CaCl_2$-type SiO_2	
		Exp.	Calc.	Exp.	Calc.
110		2.810	2.8111	2.789	2.792
011		*	2.1622	*	2.160
101				**	2.143
020		*	1.9878	**	2.000
200				**	1.948
111		1.898	1.8995	1.888	1.889
120		1.781	1.7779	1.778	1.780
210				1.750	1.752
121		1.464	1.4634	1.461	1.462
211				1.446	1.447
220		1.404	1.4056	1.394	1.396
	a axis (Å)		3.9755 (3)		3.8971 (7)
	b axis (Å)		3.9755 (3)		4.0008 (8)
	c axis (Å)		2.5767 (8)		2.5658 (2)
	V (Å^3)		40.724 (2)		40.005 (2)

related to the onset of a transformation from stishovite to a $CaCl_2$ distortion of stishovite. At 63 GPa, the diffraction peaks that are located at ~1.45 and 1.78 Å become doublets, which the stishovite model fails to explain (Fig. 2B). Instead, the modeled spectra of the $CaCl_2$ distortion of stishovite does fit (Fig. 2C and Table 1). The occurrence of the $CaCl_2$-type SiO_2 polymorph at ~63 GPa agrees with previous experiments (*3, 5*). We checked for the occurrence of other possible SiO_2 high-pressure structural forms (*12*), but only the $CaCl_2$ form was found to be compatible with the slight spectral modification found above 54 GPa. No other spectral modifications were observed above 63 GPa to the maximum pressure of 120 GPa (Fig. 2D).

Using a similar technique, Tsuchida and Yagi (*3*) proposed a higher transition pressure of 92 to 108 GPa but reported a stishovite volume of 40.09 $Å^3$ just before the transition. This volume is comparable to that found at 53.2 GPa in this study (Table 2). Our transition pressure was also ~4 GPa higher than that proposed by Kingma *et al.* (*5*) from Raman spectroscopy. Using Ne as a quasi-hydrostatic pressure medium, they observed a phase transformation without pressure hysteresis on decompression. It is possible that, after sample laser heating, the SiO_2 is metastably quenched in the pressure stability field of the $CaCl_2$ form of stishovite. However, second-order transformations usually occur without temperature hysteresis.

Subsequent Lebail refinements were performed up to 54.8 GPa and from 63 to 120 GPa to extract cell parameters for stishovite and $CaCl_2$-type SiO_2 respectively. We report cell parameters (Fig. 3 and Table 2) together with single-crystal analysis to 16 GPa (*20*) and powder-diffraction analysis to 54 GPa (*21*). The evolution of *c/a* axes and *c/b* axes ratios (Fig. 3) shows the transition of stishovite to the $CaCl_2$ form, with an increase of the $CaCl_2$ distortion with increasing pressure to 120 GPa (Table 2). The mean value between the *c/a* axes and *c/b* axes ratios becomes almost independent of pressure above 45 GPa, with a value of ~0.651. This means that the *c* axis, which corresponds to the Si–Si distance, no longer remains less compressible than the (*a*, *b*) plane (Fig. 1). In a manner similar to that for the mean value between the *a* and *b* axes, the pressure evolution of the *c* axis does not show any significant discontinuity during the phse transformation of stishovite to a $CaCl_2$ form of SiO_2. These observations agree with previous calculations (*6, 7, 14, 22*).

The pressure evolution of the *a* and *b* cell parameters (Fig. 3) is similar to that usually found for a Landau-type temperature-induced transition (*23*). With a standard type of representation for such transition with the ratio of $(a - b)/a$ axes as an order parameter, results indicate that the $CaCl_2$ form of SiO_2 is the lower entropy polymorph. Therefore, the $CaCl_2$ form may be the low-temperature polymorph of stishovite. This indicates a pos-

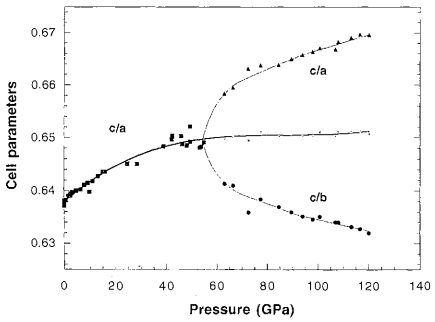

Fig. 3. Pressure evolution of the unit cell parameters showing a rapid increase of the difference between *a* and *b* axes above 54 GPa. The mean value between the *a* and *b* axes [as well as the *c* axis (Table 2)] continues without discontinuity the pressure evolution found for SiO_2 at lower pressures. Symbols correspond to *c/a* for stishovite (squares) and *c/a* (triangles), *c/b* (circles), and the mean value between *c/a* and *c/b* (gray squares) for the $CaCl_2$ form of SiO_2.

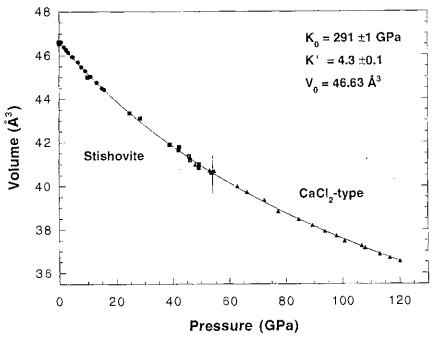

Fig. 4. EOS of silica up to CMB pressure. Circles, squares, and triangles represent data from Ross *et al.* (*20*), Hemley *et al.* (*21*), and this study, respectively. The vertical line at 54 GPa shows the transition pressure between SiO_2 and the $CaCl_2$ form of SiO_2. Within our experimental resolution of ~2 per mil, there is no significant variation of volume or compressibility above the transition pressure (see Table 3).

Table 2. Stishovite and $CaCl_2$-type SiO_2 cell parameters used to calculate equations of state up to 120 GPa. Pt volumes (V_{Pt}) were used to calculate pressure (*P*) within the x-ray spot (*13*). Only some of the previous measurements for single-crystal x-ray diffraction are reported. Numbers in parentheses are uncertainties in measured parameters.

P (GPa)	*a* axis (Å)	*b* axis (Å)	*c* axis (Å)	*V* (Å³)	V_{Pt} (Å³)
		Single-crystal x-ray diffraction (20)			
0.0001	4.1801		2.6678	46.615	
2.50	4.1667		2.6645	46.259	
4.70	4.1560		2.6601	45.946	
9.00	4.1337		2.6517	45.311	
11.0	4.1246		2.6474	45.038	
15.0	4.1043		2.6417	44.500	
		Powder diffraction (21)			
24.6	4.066		2.623	43.359	
28.5	4.058		2.618	43.100	
38.9	4.013		2.602	41.909	
42.0	4.002		2.600	41.649	
42.3	4.006		2.605	41.801	
45.8	3.992		2.596	41.368	
46.3	3.989		2.588	41.195	
49.3	3.972		2.590	40.870	
49.4	3.982		2.585	41.000	
		This study			
48.1	3.9836 (2)		2.5837 (4)	41.000	53.1754 (4)
53.2	3.9755 (3)		2.5767 (8)	40.724	52.6494 (4)
54.8	3.9725 (3)		2.5788 (9)	40.695	52.4946 (6)
63.0	3.8971 (7)	4.0008 (8)	2.5658 (2)	40.005	51.7214 (2)
66.4	3.8829 (7)	3.9955 (7)	2.5608 (3)	39.729	51.4481 (3)
72.5	3.8467 (11)	4.0114 (12)	2.5509 (4)	39.363	50.9043 (3)
77.5	3.8325 (9)	3.9848 (10)	2.5438 (2)	38.848	50.5039 (3)
84.6	3.8170 (10)	3.9787 (11)	2.5339 (2)	38.481	49.9557 (2)
89.5	3.8014 (10)	3.9750 (11)	2.5279 (2)	38.198	49.6002 (3)
93.9	3.7882 (9)	3.9709 (10)	2.5221 (2)	37.939	49.2878 (3)
97.9	3.7773 (10)	3.9664 (11)	2.5169 (3)	37.709	49.0135 (3)
101	3.7675 (6)	3.9576 (7)	2.5130 (2)	37.469	48.8210 (2)
107	3.7592 (6)	3.9537 (7)	2.5069 (2)	37.259	48.8746 (2)
108	3.7505 (7)	3.9533 (8)	2.5065 (3)	37.164	48.3612 (3)
113	3.7364 (7)	3.9482 (8)	2.4998 (2)	36.876	48.0360 (2)
117	3.7270 (8)	3.9449 (9)	2.4960 (3)	36.699	47.8328 (3)
120	3.7201 (8)	3.9422 (9)	2.4913 (3)	36.535	47.6216 (2)
0.0001*	4.1803 (2)		2.6635 (7)	46.545	60.5684 (3)

*SiO_2 obtained after a rapid quench from 120 GPa.

itive slope of the boundary between the two silica polymorphs in a pressure-temperature (P-T) diagram. The critical temperature of the phase transition [$T_c(P)$] would reach T = 300 K when pressure reaches 54 GPa. This means that, while further compressing silica at room temperature (T_{exp}) above 54 GPa, we increase the gap between the experimental and critical temperatures [the gap is ($T_c - T_{exp}$)]. For such a second-order transition, an increase in ($T_c - T_{exp}$) explains the increase of the $CaCl_2$ distortion that we observed.

There is no substantial discontinuity in the volume of the SiO_2 polymorphs at the transition pressure (Fig. 4 and Table 2), which indicates that the volume difference between stishovite and $CaCl_2$-type SiO_2 is either negligible or below the experimental resolution of ~2 per mil. This resolution also corresponds to an imprecision in the integrated transition energy of ~1.5 kJ/mol ($P\Delta V_{error}$) (V, molar volume). This imprecision is higher than energies that are commonly encountered in Landau-type transitions involving octahedral rotations, which are usually hundreds of joules per mole (*24*). Thus, a volume variation below our resolution can balance the integrated loss of free energy that is related to the formation of the lower entropy $CaCl_2$ form of SiO_2.

We calculated various third-order Birch-Murnaghan equations of state for the different sections of the compression curve (Table 3). In the experimental accuracy, there is no significant EOS variation when considering pressures up to 53.2 or 120 GPa. We therefore propose the same EOS for the high-pressure silica forms from 1 bar to 120 GPa, with the zero-pressure bulk modulus K_0 = 291 ± 1 GPa, the first pressure derivative of the bulk modulus $K' = \partial K/\partial P$ = 4.29 ± 0.05, and the unit cell volume of stishovite in standard conditions V_0 = 46.629 ± 5 Å^3. Looking at minor effects, we note that a slightly lower bulk modulus (K_0 = 282 ± 1 GPa; K' = 4.29 fixed) is associated with a slightly larger room pressure volume, when considering the experimental data for the $CaCl_2$ form of SiO_2 only (Table 3).

Table 3. EOS data for silica and SiO_6 octahedra. Errors are estimated to be 1 GPa, 0.05, and 0.005 Å^3 for K_0, K', and V_0, respectively.

P_{min} (GPa)	P_{max} (GPa)	K_0 (GPa)	K'	V_0 (Å^3)
		Stishovite		
0.0001*		306		
0.0001	15	313	4†	46.591
0.0001	53.2	291	4.29	46.629
		$CaCl_2$-type silica		
63	120	282	4.29†	46.868
		Silica		
0.0001	120	289	4.41	46.635
0.0001	120	291	4.29†	46.630
		SiO_6 octahedra		
0.0001	53.2	319	3.32	11.190
0.0001	53.2	303	4†	11.198
0.0001	120‡	312	4.95	11.190
0.0001	120‡	346	4	11.169

*Brillouin scattering measurements (*25*). All other calculations are with the low-pressure single-crystal diffraction data (*20*). †Fixed. ‡Experimental data between 15 and 63 GPa were excluded.

We then extracted atomic coordinates with the Rietveld method, which compares the experimental and modeled intensities of Bragg lines. There are one or two parameters for determining the oxygen position in stishovite (x, x, 0) or $CaCl_2$-type SiO_2 (x, y, 0), respectively. The calculations converged to atomic positions (Table 4) that agreed between experimental and calculated features (see Fig. 2), with standard deviations between 0.7 and 1.5 and between 3 and 7% for the χ^2 and $R(F^2)$ parameters, respectively. We observed a slight preferred orientation away from the c axis for both SiO_2 polymorphs. We obtained a better agreement between the calculated and experimental features by considering a thermal parameter for silicon that was about twice that for oxygen.

In the stability field of stishovite, we first note the higher compression of the polar Si–O bond in comparison with the equatorial bond (Figs. 1 and 5A), which is consistent with the single-crystal diffraction measurements by Ross *et al.* (*20*) and with the calculations by Karki *et al.* (*7*). At about the transition pressure (54 GPa) between stishovite and $CaCl_2$-type SiO_2, the polar Si–O bond becomes shorter

Table 4. Oxygen coordinates up to 120 GPa and data for Si–O, O–O, and V_{octa}.

P (GPa)	x axis	y axis	SiO (2, Å)	SiO (4, Å)	V_{octa} (Å^3)	O–O_{min} (Å)
			Single-crystal x-ray diffraction (20)			
0.0001	0.3067		1.8130	1.7560	11.181	2.2854
2.50	0.3061		1.8016	1.7554	11.103	2.2852
4.70	0.3062		1.8000	1.7512	11.040	2.2781
9.00	0.3057		1.7873	1.7458	10.895	2.2717
11.0	0.3057		1.7829	1.7428	10.831	2.2667
15.0	0.3053		1.7721	1.7383	10.709	2.2602
			Powder Rietveld refinement (this study)			
48.1	0.306		1.724	1.692	9.873	2.186
53.2	0.306		1.721	1.688	9.804	2.180
54.8	0.302		1.697	1.703	9.840	2.225
63.0	0.283	0.323	1.699	1.692	9.726	2.206
66.1	0.283	0.323	1.695	1.688	9.660	2.200
72.5	0.281	0.321	1.680	1.690	9.591	2.216
77.5	0.281	0.324	1.682	1.677	9.461	2.186
84.6	0.285	0.320	1.676	1.670	9.348	2.176
89.5	0.279	0.317	1.649	1.682	9.328	2.219
93.9	0.281	0.317	1.649	1.675	9.253	2.205
97.9	0.276	0.311	1.616	1.691	9.243	2.260
101	0.275	0.322	1.642	1.671	9.176	2.204
107	0.275	0.325	1.648	1.664	9.123	2.188
108	0.278	0.323	1.650	1.658	9.077	2.173
113	0.275	0.315	1.613	1.674	9.042	2.228
117	0.271	0.312	1.593	1.684	9.028	2.260
120	0.276	0.313	1.605	1.670	8.956	2.225
0.0001	0.308		1.819	1.751	11.587	2.274

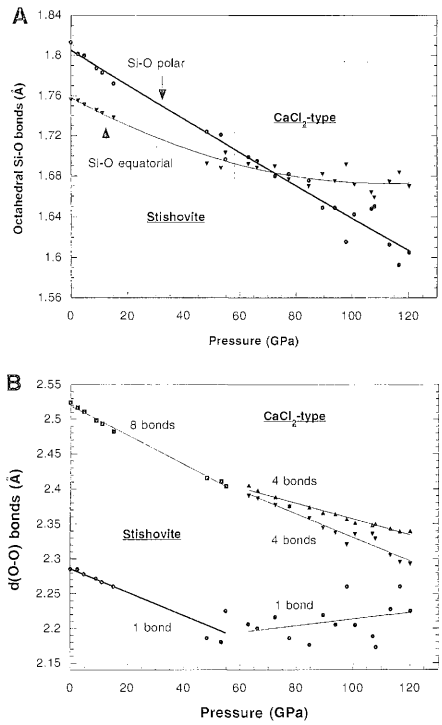

Fig. 5. The occurrence of the $CaCl_2$-type stishovite distortion is associated with (**A**) a progressive inversion of the shortest Si–O distance from equatorial (triangles) to polar bonds (circles) and (**B**) a change in compression of the shortest O–O bond distance (circles), allowing all the shortest O–O bond distances to evolve toward a similar value of ~2.25 to 2.30 Å for the highest pressures and resulting in a more symmetrical oxygen sublattice. Squares, stishovite; triangles, $CaCl_2$-form O–O bonds.

than the equatorial bond. We also note a change in the pressure evolution of the shortest O–O distance above the transition pressure (Fig. 5B). In the $CaCl_2$ structure, the compression occurs without a further decrease of this short O–O distance, but instead, the O–O first distances evolve toward a comparable value (that is, the oxygen sublattice becomes more symmetrical).

The modification of the a and b cell parameters above 54 GPa is achieved by a rapid rotation of the SiO_6 octahedra in the (a, b) plane, as supported by the pressure evolution of the (x, y, 0) oxygen coordinates (Table 4). The octahedral volumes are calculated from the set of SiO bond lengths. The octahedral bulk moduli, with single-crystal data (*20*) and pressures below 53.2 GPa or above 63 GPa were found to be significantly different in stishovite and $CaCl_2$ forms of SiO_2 (Table 3). Our results are compatible with an integrated octahedral volume variation of about +1% between stishovite and $CaCl_2$-type SiO_2 above the transition pressure (this integrated volume is a volume excess that is built across the second-order phase transformation). This volume variation does not affect the unit cell volume because other structural entities compensate for this volume excess. This suggests that, in stishovite, the SiO_6 compression is high and that the octahedral volume relaxes in the $CaCl_2$ form of SiO_2. We thus propose that, when it adopts the *mmm* point group, the ideal SiO_6 octahedral K_0 is that calculated for the $CaCl_2$ form of SiO_2 (K_0 = 311 ± 1; K' = 4.95 ± 0.05).

The integrated 1% volume variation of SiO_6 octahedra (ΔV_{octa}) corresponds to a compression work of ~35 kJ ($P\Delta V_{octa}$), which is much higher than the maximal integrated energy variation that is involved in the transition of <1.5 kJ/mol. This suggests an energy exchange between SiO_6 octahedra and other polyhedra of the lattice during the phase transition. A similar redistribution could also affect thermal energy. For example, with the entropy change that is related to the pressure evolution of the (a – b)/a–order parameter, there might be an entropy gain that is related to the achievement of a more symmetrical oxygen sublattice (Fig. 5B).

We observed a continuous increase of the SiO_2 density up to the pressures of Earth's CMB (Fig. 4). We coupled this EOS (Table 3) with those that were previously reported in similar experimental conditions for $MgSiO_3$ (V_0 = 162.6 Å^3, K_0 = 256 GPa, and K' = 4) (*17*) and MgO (V_0 = 74.70 Å^3, K_0 = 167 GPa, and K' = 4.5) (*15*). We calculated that the ΔV value that is related to the $MgSiO_3 \rightarrow MgO + SiO_2$ breakdown reaction is positive at all pressures. At 300 K, ΔV increases from ~1 to 4% of the perovskite volume between 25 and 120 GPa, respectively. It might be argued that high-temperature conditions or minor elements can reverse this sign, but so far no such inversion has been observed in high-pressure experiments. Therefore, silicate perovskite is denser than a mixture of its oxides down to the CMB. Consequently, the proposal that free silica could occur in Earth's lower mantle is not supported by the present data, so lor[illegible] an excess of magnesiowüstite (Mg,Fe)O is thought to be present in the lower mantle.

References and Notes

1. J. Haines, J.-M. Léger, O. Schulte, *J. Phys. Condens. Matter* **8**, 1631 (1996).
2. At the CMB, pressure and temperature are 135 GPa and between 3000 and 4000 K, respectively. Experimental results suggested that $MgSiO_3$ breaks down into MgO periclase and SiO_2 above 58 GPa [S. K. Saxena *et al.*, *Science* **274**, 1357 (1996)].
3. Y. Tsuchida and T. Yagi, *Nature* **340**, 217 (1989).
4. J. K. Kingma, H. K. Mao, R. J. Hemley, *High Pressure Res.* **14**, 363 (1996).
5. J. K. Kingma, R. E. Cohen, R. J. Hemley, H. K. Mao, *Nature* **374**, 243 (1995).
6. R. E. Cohen, in *High-Pressure Research: Application to Earth and Planetary Sciences*, vol. 67 of *Geophysical Monograph Series*, Y. Syono and M. H. Manghnani, Eds. (American Geophysical Union, Washington, DC, 1992), pp. 425–431.
7. B. B. Karki, M. C. Warren, L. Stixrude, G. J. Ackland, J. Crain, *Phys. Rev. B* **55**, 3465 (1997).
8. J. S. Tse, D. D. Klug, Y. Le Page, *Phys. Rev. Lett.* **69**, 3647 (1992).
9. D. J. Lacks and R. G. Gordon, *J. Geophys. Res.* **98**, 22147 (1993).
10. A. El Goresy, L. Dubrovinsky, S. Saxena, T. G. Sharp, *Meteoritics* **33** (suppl.), A45 (1998).
11. L. G. Liu, *Earth Planet. Sci. Lett.* **49**, 166 (1980).
12. J. Haines, J. M. Léger, O. Schulte, *Science* **271**, 629 (1996).
13. J. C. Jamieson, J. N. Fritz, M. H. Manghnani, in *High-Pressure Research in Geophysics*, Y. Akimoto and M. H. Manghnani, Eds. (Reidel, Boston, MA, 1982), pp. 425–431.
14. J. Haines, J.-M. Léger, S. Hoyau, *J. Phys. Chem. Solids* **56**, 965 (1995).
15. G. Fiquet, D. Andrault, J.-P. Itié, P. Gillet, P. Richet, *Phys. Earth Planet. Inter.* **95**, 1 (1996).
16. D. Andrault, G. Fiquet, M. Kunz, F. Visocekas, D. Häusermann, *Science* **278**, 831 (1997).
17. G. Fiquet *et al.*, *Phys. Earth Planet. Inter.* **105**, 21 (1998).
18. J. Hammersley, *Publication No. ESRF98HA01T* (ESRF, Grenoble, France, 1996).
19. A. C. Larson and R. B. Von Dreele, *GSAS Manual* (Los Alamos National Laboratory, Los Alamos, NM, 1994), pp. 86–748; A. LeBail, in *Accuracy in Powder Diffraction*, E. Prince and J. K. Stalick, Eds. (National Institute of Standards and Technology, Gaithersburg, MD, 1992), p. 213.
20. N. L. Ross, J. F. Shu, R. M. Hazen, T. Gasparik, *Am. Mineral.* **75**, 739 (1990).
21. R. J. Hemley, C. T. Prewitt, K. J. Kingma, in *Silica: Physical Behavior, Geochemistry and Materials Applications*, P. J. Heaney, C. T. Prewitt, G. V. Gibbs, Eds. (Mineralogical Society of America, Washington, DC, 1994), pp. 41–81.
22. R. E. Cohen, *Am. Mineral.* **76**, 733 (1991).
23. E. K. H. Salje, *Phase Transitions in Ferroelastic and Co-Elastic Crystals* (Cambridge Univ. Press, New York, 1990).
24. F. Guyot, P. Richet, P. Courtial, P. Gillet, *Phys. Chem. Miner.* **20**, 141 (1993); D. de Ligny and P. Richet, *Phys. Rev. B* **53**, 3013 (1996).
25. D. J. Weidner, J. D. Bass, A. E. Ringwood, W. Sinclair, *J. Geophys. Res.* **87**, 4740 (1982).

26. We thank T. Charpin, P. Richet, N. L. Ross, and two anonymous referees for their help and comments. D.A. thanks M. Kunz and L. W. Finger for their help with the GSAS code. This work was supported by the CNRS Institut National des Sciences de l'Univers, Institut de Physique du Globe, and ESRF programs.

7 July 1998; accepted 16 September 1998

Thermodynamics of Calcite Growth: Baseline for Understanding Biomineral Formation

H. Henry Teng, Patricia M. Dove,* Christine A. Orme, James J. De Yoreo

The complexity of biomineralized structures suggests the potential of organic constituents for controlling energetic factors during crystal synthesis. Atomic force microscopy was used to investigate the thermodynamic controls on carbonate growth and to measure the dependence of step speed on step length and the dependence of critical step length on supersaturation in precisely controlled solutions. These data were used to test the classic Gibbs-Thomson relationship and provided the step edge free energies and free energy barriers to one-dimension nucleation for calcite. Addition of aspartic acid, a common component in biomineralizing systems, dramatically affected growth morphology and altered the magnitude of the surface energy.

Many organisms mediate inorganic crystallization by selective application of organic compounds (*1*–*3*) to exert detailed control over the structure (*3*), orientation (*1*), growth kinetics (*2*), and nucleation sites (*4*) of inorganic crystals. An understanding of physical controls on biomineralization promises new routes to the controlled synthesis of complex crystalline structures for application across a broad spectrum of materials-based technologies. Because it occurs ubiquitously among biomineralizing systems (*5*) and it is easily crystallized, calcite—often in combination with aspartic acid–rich protein mixtures (*1*, *2*,